Supplemental Material

Greg Bubnis, Herre Jelger Risselada, and Helmut Grubmüller
(Dated: August 29, 2016)

CONTENTS

PUBLISHED κ VALUES FOR MARTINI LIPIDS

Table S1 presents published κ values for Martini lipids as well as those computed here (all assumed to be in the low curvature limit).

TABLE S1. Published κ values for Martini lipids. Simulated temperatures T[K] are indicated. κ values were adjusted to 310K using the conversion in [1], with $\mathcal{R} = 4.59$. Method abbreviations are: PR umbrella sampling (PRUS), height fluctuations (HF), field-theoretic umbrella sampling (FTUS), tether extraction (TE), tilt fluctuations (TF), simulated buckling (SB). *[2] used slightly modified unsaturated bond parameters and T was not reported (310K is assumed).

Ref.	Lipid, T[K]	$\kappa[10^{-20}J]$	$\kappa[k_BT, 310K]$	method
-	DOPE, 310		16.9±1.5	PRUS
-	DOPC, 310		23.9±1.3	PRUS
[3]	DOPC, 300	5.5±1.0	11±2.1	HF
[4]	DOPC, 310		19±4	FTUS
[2]*	DOPC	7-20	16-47	TE
-	DSPC, 310		37.7±1.7	PRUS
-	DPPC, 310		29.5±0.9	PRUS
[5]	DPPC, 323	4±2	10±5	HF
[6, 7]	DPPC, 323	8	22	HF
[8]	DPPC, 325	6.6-11	18-30	HF
[9]	DPPC, 325	15	41	TF
-	DMPC, 310		22.7±0.7	PRUS
[10]	DMPC, 300	15	31	HF
[11]	DMPC, 300	16.6±0.5	34.5±1.0	HF
[1]	DMPC, 300	12.0±0.4	24.9±0.8	SB
[1]	DMPC, 300	11.5±0.8	23.9±1.7	SB

MD SIMULATION METHODS

Simulations were performed using the Martini version 2.2 coarse grained (CG) lipid forcefield [12] which maps groups of heavy atoms into pseudoatomic beads at a 4:1 ratio. Water CG beads are isotropic and represent four water molecules. Our initial system consisted of a 1066 lipid DOPC (14 CG beads per lipid) bilayer in a half-cylinder geometry and 43444 water beads in a box of xyz dimensions 14 x 32.5 x 15 nm.

Molecular dynamics (MD) simulations were performed using GROMACS version 4.07 [13]. Simulations used a timestep of 40ps and the neighborlist was updated every 10 steps. Temperature was set to 310K with separate Berendsen thermostats for the lipids and solvent, both with a coupling time of 1 ps. Pressure was set to 1 bar with the Berendsen coupling scheme with a time constant of 4 ps. Semi-isotropic pressure coupling was used to constrain the z dimension while allowing the x and y dimensions to vary normally. For this, compressibilities of 3e-5 bar^{-1} and 0 were used for the xy plane and z dimension, respectively. The membrane's translational and rotational center-of-mass motion were removed at every integration step. Van der Waals interactions were cut off at 1.2nm with a switch function beginning at 0.9 nm. Coulomb interactions were cut off and shifted at 1.2nm and used a relative permittivity of 15.

The initial DOPC structure (shown in Fig. 1(a)) was prepared by allowing a halved cylinder to fully relax (unbend) and then bending it back beyond its starting point. The intial half cylinder was simulated for 100 ns then PR was performed on the trajectory from 4-100 ns, at 200 ps intervals with $d' = 1.6$nm, and the 4 ns frame as $\mathbf{x}^{\mathrm{ref,PR}}$. From this permuted trajectory, $\tilde{\mathbf{x}}(t)$, the first PCA mode, ξ, (considering all lipid PO4 beads) was taken as a bending coordinate. To bend the membrane further, starting from the t=4.4 ns frame, acceptance linear expansion was used on the ξ coordinate. This non-equilibrium method (detailed in the Gromacs documentation) accepts integration steps only in the desired directon along ξ. During bending, PR was done every 40ps with $d' = 1.6$nm and $\langle\tilde{\mathbf{x}}(t)\rangle$ (averaged over 4-100ns) as the reference $\mathbf{x}^{\mathrm{ref,PR}}$. A frame taken during bending, (shown in Fig. 1(a)) was then used to initiate the unbending pathway described in the main text. The previous average $\langle\tilde{\mathbf{x}}(t)\rangle$, being between the bent/flat extremes, was used as the reference for PR of the unbending pathway described in the main text.

Because DOPC, DOPE, and DSPC have identical topologies (coarse grained), the DOPE and DSPC ensembles were generated trivially from the production DOPC ensemble by using the same initial structures, umbrella/PR reference structures, and collective coordinate while only changing the appropriate bead identities and bond parameters. Switching DOPC's NC3 headgroup bead to NH3 yields DOPE. Changing DOPC's D3A/D3B tail beads (unsaturated) to aliphatic C3A/C3B beads yields DSPC. Following 50 ns of equilibration per umbrella window, production data was collected.

DPPC and DMPC umbrella ensembles were created beginning from a highly curved DSPC geometry with the excess tail beads changed to water beads. With position restrained lipid PO4 beads (k=5kJ/mol-nm^2 for DPPC, 1kJ/mol-nm^2 for DMPC) the system was relaxed by steepest descent, and then a brief (2 ns for DPPC, 12 ns for DMPC) equilibration was performed with a shorter timestep, dt=20 fs, to allow water to exit the hydrophobic interior region. The position restraints were then removed, and the unbending-bending process described above for DOPC was used to prepare the initial, highly-bent DPPC and DMPC structures. Subsequent relaxation, PR, PCA, and production simulations used the same parameters as for DOPC except that only the first 50ns was used for PCA because DPPC and DMPC relaxed more quickly to flat membranes.

PMF CALCULATIONS

PMF uncertainties were estimated using the bootstrapping scheme implemented in g_wham [14], which first computes the integrated autocorrelation time, τ_l for each window l, and then resamples $\xi(t)$ according to τ_l. Bootstrapping was repeated to give 30 PMFs from which means and standard deviations were be computed.

CANHAM-HELFRICH ENERGIES, TRANSFER FUNCTIONS, κ AND μ

To recast the computed free energy $E(\xi)$ in the Canham-Helfrich framework, two transfer functions, $H_2(\xi)$ and $H_4(H_2)$, were required to compute the free energies $E_2(H_2)$ and $E_4(H_4)$ and the corresponding elastic moduli, κ and μ. The transfer functions are needed to properly account for entropic effects in the change of coordinates (see e.g. [15]).

This was done in two stages: i) $E(\xi)$ was transferred to $E(H_2)$ which was then split into a linear term $E_2(H_2)$ and an excess energy $E_4(H_2)$; and ii) the excess $E_4(H_2)$ was transferred to $E_4(H_4)$. The transfer functions, $H_2(\xi)$ and

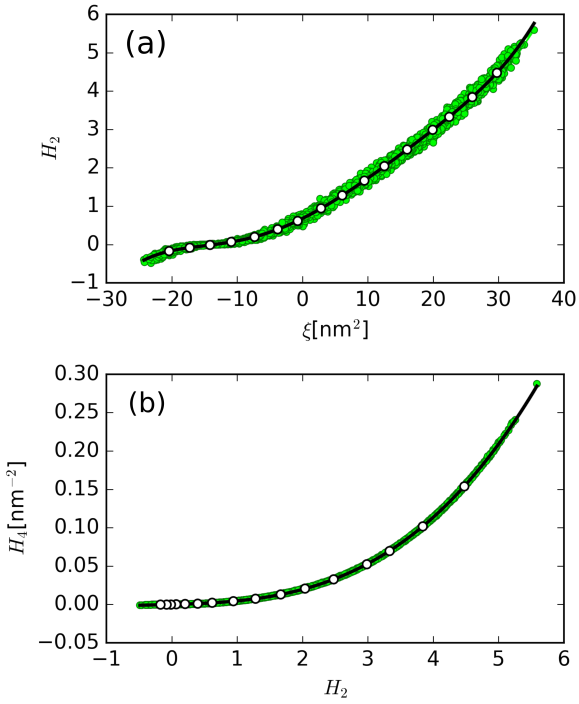

FIG. S1. Transfer functions (a) $H_2(\xi)$ and (b) $H_4(H_2)$ for the DOPC production ensemble. The full ensemble is plotted as green dots. The black lines in (a) and (b) are fifth and third order polynomial fits, respectively. For each umbrella window, a white dot shows $\langle\xi\rangle$ and $\langle H_2\rangle$ in (a) and (b), respectively.

$H_4(H_2)$, shown in Fig. S1, were derived from the full umbrella ensemble, and, to ensure that they were invertible, the ordinate values of H_2 and H_4 were signed by the mean curvature to distinguish cases of slight negative (downward facing in this setup) curvature from positive.

The first transfer from $E(\xi)$ to $E(H_2)$ was calculated as in [15] via:

$$E(H_2) \ = E(\xi) + k_B T \ln \frac{dH_2(\xi)}{d\xi} \tag{S.1}$$

where $H_2(\xi)$ was a fifth order polynomial fit and the second term is the entropic correction requiring an invertible transfer function. $E_4(H_4)$ was calculated similarly, from $E_4(H_2)$, but with the transfer function $H_4(H_2)$ being a third order polynomial fit.

The (quadratic) bending modulus κ was determined from $E_2 = (\kappa/2)H_2$, the linear component of the CH bending energy. Then, using $E_4 = (\mu/4)H_4$, the quartic modulus μ was extracted from a linear fit of $E_4(H_4)$ (shown in Fig. S2). The fit was applied, however, only where $E_4(H_4) > 5k_BT$. This was rationalized because the quartic energy is only relevant at higher curvatures and the low values of $E_4(H_4)$ are likely skewed by the near zero slope of $H_4(H_2)$ near the origin.

In practice, these entropic corrections are small, adding at most 2 or 4 k_BT to $E_2(H_2)$ and $E_4(H_4)$, respectively. If these terms are disregarded, κ decreases by $< 2k_BT$ and the quartic modulus μ does not change significantly. So while being technically appropriate, these correction terms only yield slight, nearly neglectable, adjustments to our numerical results.

CYLINDRICAL TETHERS AND HEIGHT FLUCTUATION SPECTROSCOPY CALCULATIONS OF κ (FOR DOPC)

To validate our PRUS results, here we compute κ for DOPC using two independent controls at the curvature extremes: cylindrical tethers (CT) [16, 17] with curvature radii of 4-9nm, and height fluctuation (HF) spectroscopy [18] for vanishing ($R >$100nm) curvatures. The results are summarized in Fig. S3, which shows CT, HF, and PRUS values of κ for DOPC. Details of the CT and HF calculations are as follows.

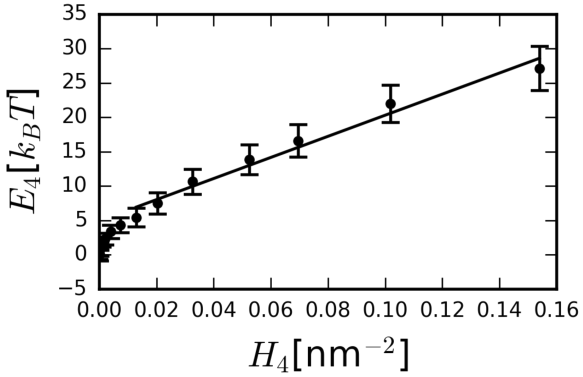

FIG. S2. The quartic bending energy, $E_4(H_4)$ for DOPC. Error bars are 95% confidence intervals and the linear fit considers only points with $E_4 > 5k_BT$.

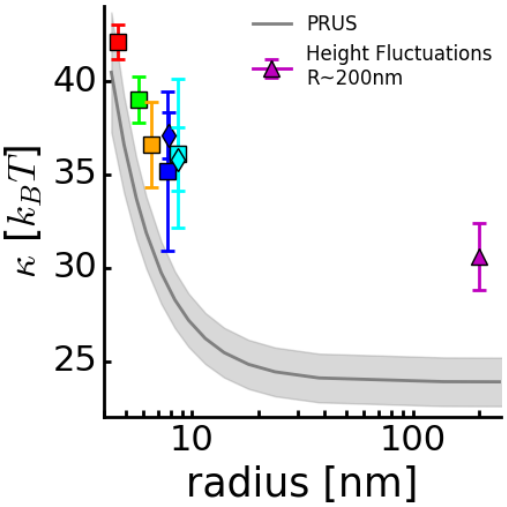

FIG. S3. κ computed via CT, HF, and PRUS methods. CT data are shown as squares and diamonds, the HF estimate as a triangle, and PRUS as a grey line. Uncertainties are 95% confindence intervals.

Cylindrical Tethers

In the simulated tether scheme, κ can be derived from a membrane cylinder's axial tension and its radius. For details of the theory, see the original reference [16] and a more recent application to Martini lipids [17].

Our simulations differed from the others mainly in our approach to facilitate equilibration of lipids/solvent between the inner and outer leaflets/regions. Here, each tether included a rigid 'stick' which stabilized, on opposite sides of the cylinder, two hydrophobic defects (pores) through which solvent and lipid headgroups could freely pass. The sticks were comprised of (non-canonical) particles (colored red in Fig. S4) that were repulsive to lipid tails (Lennard-Jones parameters σ =1.10 nm, and,ϵ =0.01 kJ/mol) but non-interacting with all other particles. To avoid spurious contributions to pressure or temperature, the atoms comprising the sticks were 'frozen' during simulations, meaning they had fixed positions and did not interact with the thermostat or barostat. Being uncoupled and static, the sticks served as a localized field potential to repel only lipid tails, mimicking the method in [17]. Each stick comprised 75 atoms, spanning the full L_x box dimension so as to avoid any boundary effects. Otherwise, the tether simulations used the same pressure and temperature coupling schemes as the PRUS simulations, but a shorter timestep dt =25fs was used.

We prepared tethers with 2,132 DOPC lipids and 76,557 waters with radii R = 4.6, 5.7, 6.5, 7.7 and 8.6 nm. Two

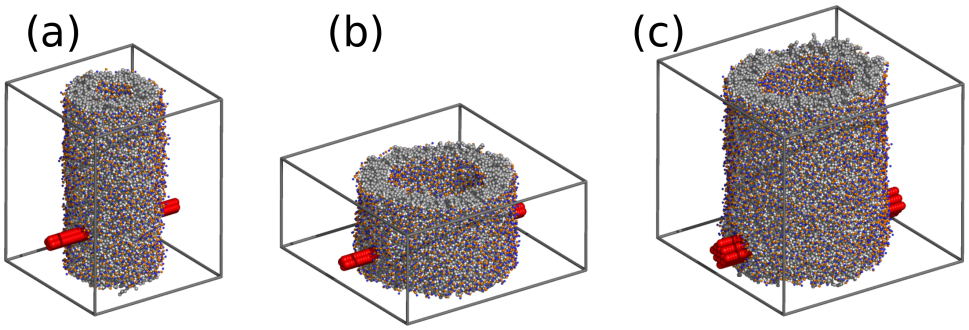

FIG. S4. Three CT starting configurations with radii (a) 4.6nm, (b) 8.6nm, and (c) 8.7nm. The tethers (a) and (b) are single systems of 2,132 DOPC lipids whereas (c) is a double stack with 4,264 lipids. For clarity, waters are not drawn. The sticks, repulsive only to lipid tails and non-interacting with all other particles, are colored red.

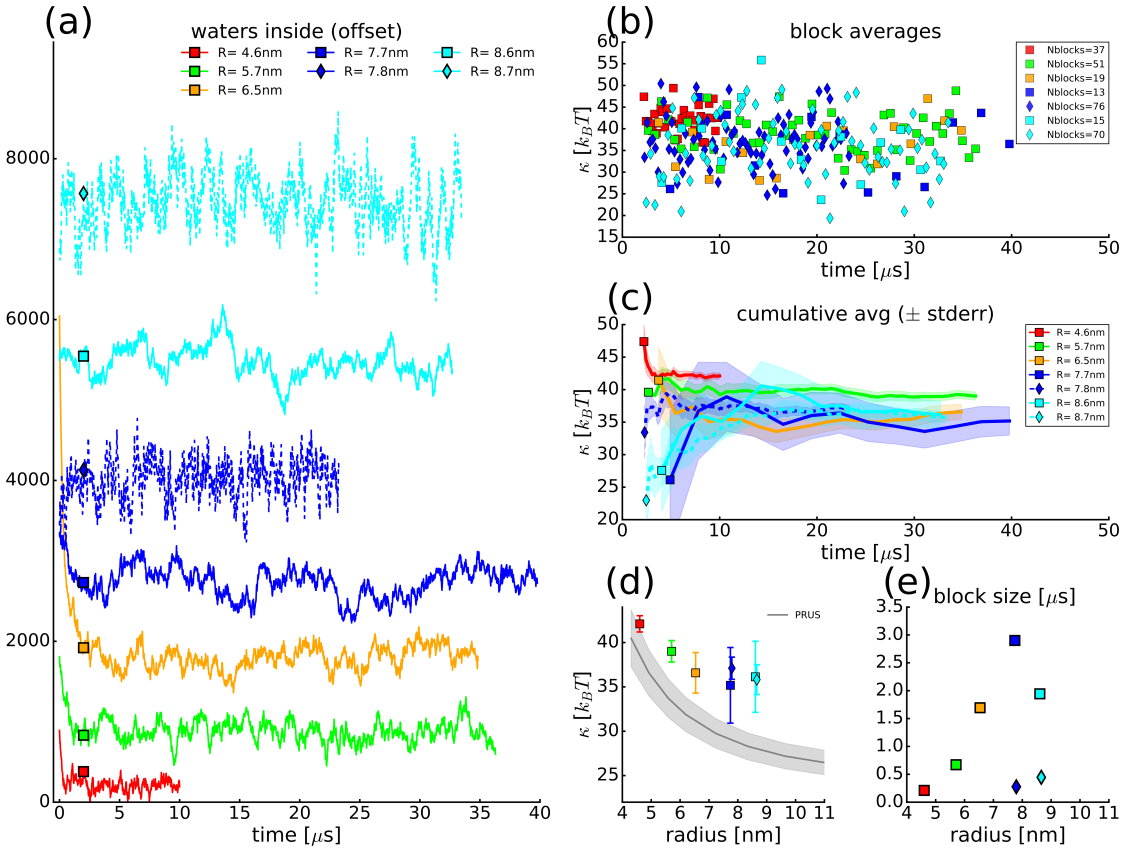

FIG. S5. κ computed via CT simulations. (a) Water counts, offset vertically for visual clarity (values are relative). (b) block average values of κ. The legend indicates the number of blocks, estimated via autocorrelation analysis, for each tether system. (c) Cumulative averages of κ for each tether, the shaded bands indicate standard errors from block averaging. (d) Comparison of CT κ values to PRUS. Uncertainties are 95% confidence intervals (e) Block sizes estimated via autocorrelation analysis of data in (a). In all panels, square symbols and solid lines signify the 2,132 lipid systems whereas diamonds and dashed lines signify the double-stacked 4,264 lipid systems.

examples are shown in Fig. S4 (a) and (b). For the shorter tethers (R = 7.7 and 8.6nm), where axial periodicity artefacts could arise, we also prepared double-stacked systems having twice the lipid/solvent count but still only two pores, for example Fig. S4 (c). To speed equilibration, sticks were bundled to achieve pore radii of 1.5 and 2.6 nm in the regular and double-stacked systems, respectively.

Tethers were equilibrated for a minimum of 2 μs before any production data was collected. Following equilibration, water flux in and out of the cylinder was found to have large amplitude fluctuations on μs timescales, whereas lipid

exchange was much faster. Autocorrelation times – computed with the method of [19] as implemented in the pymbar python package – for the water count inside the tether were thus used to set appropriate block lengths for block averaging statistics of κ.

To compute $\kappa = f_{zz}R/2\pi$, the tether radius R was computed as the radius of gyration of the lipids' terminal (C5A) tail beads (projected onto the xy plane), and the axial force was computed as $f_{zz} = (P_{zz} - (P_{xx} + P_{yy})/2)L_xL_y$, where P_{xx}, P_{yy}, P_{zz} are diagonal terms of the pressure tensor and L_x,L_y are box dimensions.

The results of the CT simulations are summarized in Fig. S5. Overall, as seen in panel (d), as R increases from 4.6 to 7nm, κ follows a well converged, monotonic decreasing trend, shifted about 5 k_BT above the PRUS values in grey. This CT convergence is consistent with the well-sampled water fluctuations in (a), the plateaued cumulative averages of κ in (c), and the short block sizes in (e).

In contrast, as R increases above 7nm (blue and cyan data), the convergence worsens considerably. Two main reasons are: i) decreasing axial stress gives a worsening signal-to-noise ratio and ii) water fluctuations, with increasing amplitudes, are coupled to slow radial breathing modes of the cylinder. Indeed, the 2,132 lipid systems both show very slow water fluctuations in Fig. S5(a), large uncertainties in (b), and large block sizes in (e).

In an effort to speed water equilibration, the double stack systems used larger stick bundles to stabilize larger pores. Within statistical uncertainties, however, the results of the single and doublestack systems were equivalent. In addition, the time traces for double stacks in Fig. S5(a) show large fluctuations occuring on disparate timescales, and it is likely that the autocorrelation times (sub-500ns block sizes in panel (e)) are large under-estimates.

For tethers beyond R=7nm, a more advanced analysis, perhaps accounting for fluctuations or other systematic effects might be required to reliably compute κ. Accordingly, we elected not to pursue such efforts at these intermediate R values, but rather to carry out a HF control at the very large R (vanishing curvature) limit.

Height Fluctuation Spectroscopy

The HF membrane system comprised 5,000 DOPC lipids and 179,115 waters, in a 40.1×40.1×17.7 nm box. The same pressure and temperature coupling settings were used as for PRUS, except that here the z dimension was not constrained. Accordingly a compressibility of 3e-5 bar^{-1} was used in both the xy and z components of the semi-isotropic pressure scheme. This setup yields a vanishing average surface tension of 5e-9 N/m, which does not to dampen large wavelength height fluctuations.

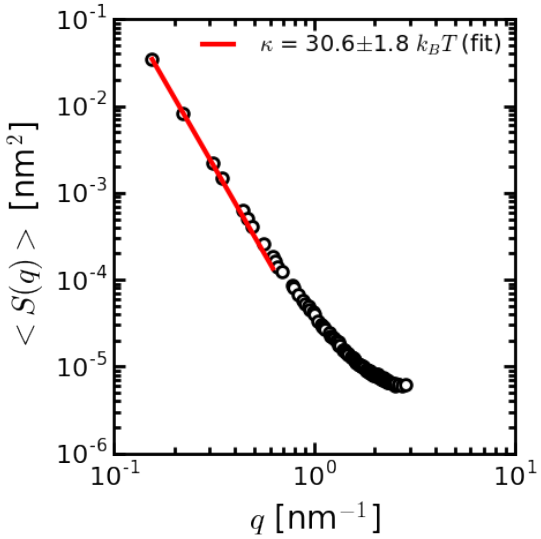

FIG. S6. $< S(q) >$ computed via HF. The fit to $< S(q) >$ for the nine lowest q, yielding κ=30.6k_BT is shown in red. The uncertainty (95% confidence interval) of 1.8 k_BT was estimated from four block averages of κ.

The first 400ns of simulation was discarded for equilibration. In the subsequent production run of 3800ns, lipid coordinates were stored at 2ns intervals. At each frame, the $z(x, y)$ surface of the midplane was computed on a 28×28 grid, using the discretization scheme of [8] applied to lipid PO4 beads. Then, $z(x, y)$ was recast as a discrete Fourier

series, yielding structure factors $S(q)$ which were averaged over equivalent wavenumbers $q = |\mathbf{q}|$. The production simulation was split into four blocks of 950ns and for each block κ was derived from a fit to $\langle S(q)\rangle = k_BT/(\kappa L^2 q^4)$ applied to wavelengths q^{-1} >10nm, where L is the lateral box length [18]. An uncertainty (95% confidence interval) in κ of 1.8 k_BT was estimated from the standard error of the block averages. Fig. S6 shows the full production average of $\langle S(q)\rangle$ and the q^{-4} fit.

CONTROL SIMULATIONS TESTING THE UMBRELLA SAMPLING PROTOCOL AND PR PARAMETERS

Here we describe additional controls used to verify that our protocol and results are insensitive to the precise choice of collective coordinate as well as PR parameters.

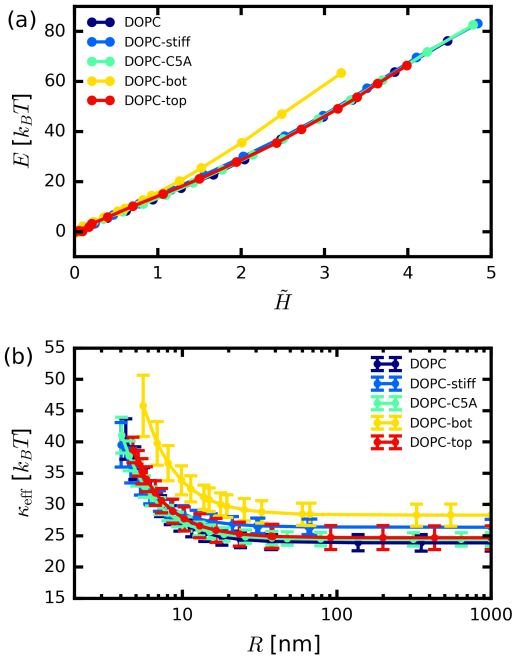

FIG. S7. Results for DOPC under different umbrella sampling restraint schemes. Relative to the DOPC production ensemble, DOPC-stiff uses $k = 3.3$ versus 1.0 kJ/(mol-nm^2), DOPC-C5A has ξ defined using C5A tail beads, DOPC-bot and DOPC-top use single leaflet restraints of PO4 beads (ξ components for only one leaflet). (a) Free energies, $E(\tilde{H})$. (b) Effective bending modulus, $\kappa_{\rm eff}$. In (a), the error bars (all $< 1.5k_BT$) were omitted for visual clarity and in (b) the error bars are 95% confidence intervals. In both panels, lines connecting points are guides to the eye.

First, we tested protocol sensitivity to the definition of the collective bending coordinate by using C5A tail beads (instead of PO4 head beads) or single leaflet restraints. PR, however, was still performed using the PO4 beads, since their positions best distinguish the upper and lower leaflets. Fig. S7 shows the results. The agreement of the DOPC (PO4) and DOPC-C5A ensembles indicates that the method is insensitive to whether lipid heads or tails define the bending coordinate. The DOPC-bot and DOPC-top ensembles use single leaflet PO4 restraints (ξ, with zeroed contributions from the opposite leaflet). The DOPC-top ensemble, with restraints only on the top, negative (intrinsic) curved leaflet was indistingiushible from the reference ensemble, whereas DOPC-bot, with restraints only on the bottom leaflet, caused a clear increase in $E(\tilde{H})$. This extra energy could arise from imposing area extension (stretching) in addition to bending.

Next, we repeated calcultions for DOPC with different PR parameter schemes. Fig. S8 shows these results. The free energies in panel (a), $E(\tilde{H})$, are visibly indistinguishible, and the more sensitive $\kappa_{\rm eff}$ results in panel (b) are still equivalent within statistical uncertainties. Using one global PR reference (the average of $\tilde{\mathbf{x}}(t)$, depicted in Fig. 2 (inset center)), as opposed to using local references for each umbrella window had no effect on computed energies, as the equivalence of the DOPC-oneref-1000-1.4 and DOPC-allref-1000-1.4 ensembles shows. Ensembles with PR performed every 1000 versus 10000 integration steps (DOPC-allref-1000-1.4 versus DOPC-allref-10000-1.4, respectively) also gave

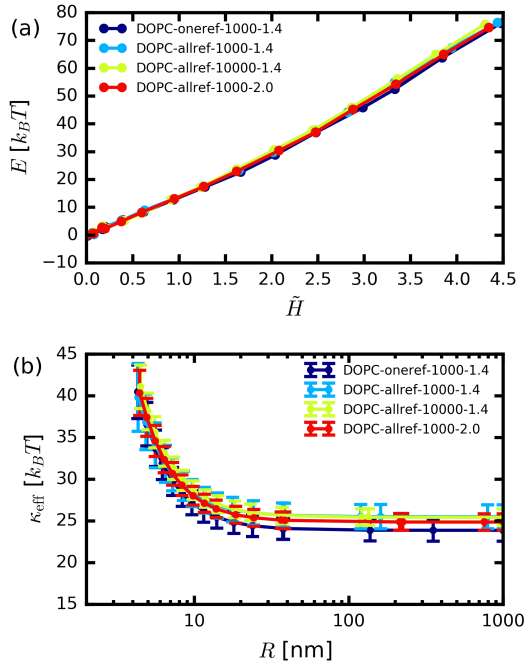

FIG. S8. Results for DOPC under different PR parameter schemes. "oneref" indicates that a single reference structure, $\mathbf{x}^{\rm ref,PR}$, was used for all umbrella windows, whereas "allref" indicates that individual, localized references (umbrella starting structures so that $\mathbf{x}^{\rm ref,PR} = \mathbf{x}^{{\rm ref},l}$) were used. The numbers 1000 or 10000 indicate the number of MD integration steps between PR and the final numbers (1.4 or 2.0) indicate d' in nm. (a) Free energies, $E(\tilde{H})$. (b) Effective bending modulus, $\kappa_{\rm eff}$. In (a), the error bars (all $< 1.5k_BT$) were omitted for visual clarity and in (b) the error bars are 95% confidence intervals. In both panels, lines connecting points are guides to the eye.

equivalent results. This also shows that PR can be performed quite infrequently, as lateral diffusion requires many integration steps. Lastly, the parameter d' does not influence results as long as it is larger than the typical lateral lipid spacing and smaller than the bilayer thickness. This is evidenced by the equivalence of results for the ensembles DOPC-allref-1000-1.4 and DOPC-allref-1000-2.0, which use d'=1.4 and 2.0nm, respectively.

COUPLING BETWEEN PERMUTATIONS AND COLLECTIVE COORDINATES

Here, the coupling between permutations and collective coordinate restraints is shown to be negligible. Whereas kinetic and potential energy are strictly invariant to lipid permutations, the restraint energy, $V_{\rm umb}$, is not. A permutation of lipids is a move in configuration space that is not strictly orthogonal to $\mathbf{v}_1$, and will therefore shift ξ and $V_{\rm umb}$. We denote a shift in ξ, resulting from PR, as $\Delta\xi^{\rm PR}$.

A direct test of whether these shifts are significant is to vary PR frequency. If $\Delta\xi^{\rm PR}$ shifts do influence (broaden) the ξ distributions collected by umbrella sampling, then increasing PR frequency would increase this effect and alter the computed free energies. However, the computed free energies and bending moduli were equivalent whether PR was done every 40 or 400 ps (see Fig. S8), suggesting the influence is negligible for this system.

We also calculated the distributions of shifts in ξ and $V_{\rm umb}$ to confirm that they were small in magnitude, and zero on average (no directional bias). Fig. S9 shows these results for the DOPC production ensemble. For all umbrella windows, the shifts $\Delta\xi^{\rm PR}$ averaged zero and had standard deviations $\leq$ 0.1nm. This distribution of shifts $p(\Delta\xi^{\rm PR})$, is about one tenth the width of the umbrella distributions $p(\xi)$ (see Fig. S9(a)). The fact that these shifts only occur when PR is performed, every 10^3 or 10^4 integration steps, likely explains why they do not significantly broaden the collected ξ distributions.

The corresponding changes in $V_{\rm umb}$ due to permutations, $\Delta V_{\rm umb}^{\rm PR}$, are also symmetric about zero (Fig. S9(b)). The decreasing trend in distribution widths is due to the fact that a larger restraint force is required at high curvature (the lower indexed umbrella windows) and therefore $\Delta\xi^{\rm PR}$ shifts will incur larger changes in $V_{\rm umb}$. The largest effect in all windows is a standard deviation of 1 kJ/mol.

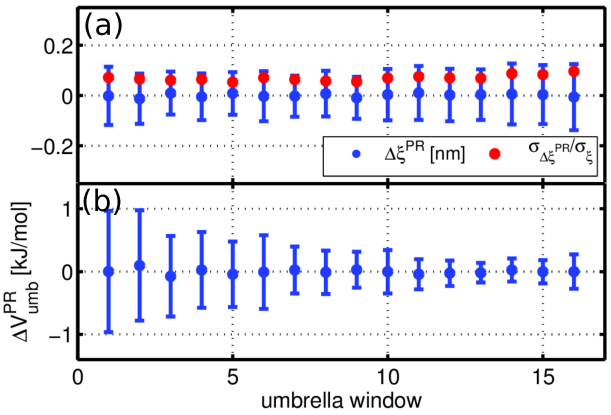

FIG. S9. (a) $\Delta\xi^{\mathrm{PR}}$ distributions for each umbrella window are shown in blue, with dots indicating means and error bars denoting $\pm\sigma$. The red dots indicate the ratio of standard deviations of the $\Delta\xi^{\mathrm{PR}}$ and ξ distributions for each umbrella window. (b) Distributions of energy shifts $\Delta V^{\mathrm{PR}}_{\mathrm{umb}}$ with means indicated as dots and error bars denoting $\pm\sigma$ Umbrella windows are sorted from highest to lowest curvature: window 1 has the highest curvature, window 14 is nearly planar and window 16 has a slight negative (downward facing) curvature.

To summarize, permutations introduce only small, symmetric shifts in ξ and V_{umb} that have no detectable influence in computed free energies. The coupling between permutations and the collective coordinate restraint is therefore weak enough to disregard.

MIDPLANE CURVATURE CALCULATION

In Fig. S10 we illustrate our approach to compute the midplane surface, from which curvature (H), area (A) and the curvature integrals are determined. The used approach accounts for two notable phenomena arising in the high curvature regime for this system (see Fig. S10). First, the membrane adopts a parabolic, rather than circular, shape, meaning curvature peaks at the center and decays moving outward, and is thus not approximately constant. Second, lipid tail splay increases the midplane area by about 10% between the flat and highly bent configurations. The full integral, $\tilde{H} = \int H^2 dA$, accounts for these effects, whereas the more convenient mean curvature approximation, $\langle H^2 \rangle \approx \langle H \rangle^2$, would be unsuitable here.

To begin, lipid coordinates are projected onto the xy plane such that $A = L_z S$, where L_z =15nm is the constrained z box length and S is the midplane arclength of the projected coordinates. Next, quadratic fits are done for the terminal tail beads (C5A for DOPC) of the top and bottom leaflets. Each C5A fit function is discretized in 50 points, evenly spaced in y and spanning the min/max values of C5A beads. The C5A bead density is computed at each point of the fit function as a sum of gaussians (of variance 1nm^2) over all beads of the respective subset (top or bottom). The leaflet endpoints are then defined where bead density falls to half its root mean square (RMS) value. The midplane surface is defined as the average of the top and bottom leaflet fits, and its length is given by the larger projection of the top and bottom leaflets. Due to tail splaying, the negative (intrinsic) curved leaflet thus sets the length, S, of the midplane interface. In the control simulations where single leaflet restraints are used (DOPC-top and DOPC-bot ensembles shown in Fig. S7), we use the midplane projection of the restrained leaflet. For the shorter 12/10 bead lipids DPPC/DMPC, the procedure is the same, except that we use fits to (terminal) C4A/C3A beads. With this midplane surface and endpoint definition, the curvature integrals $\tilde{H} = H_2 = \int H^2 dA$ and $H_4 = \int H^4 dA$ can be evaluated.

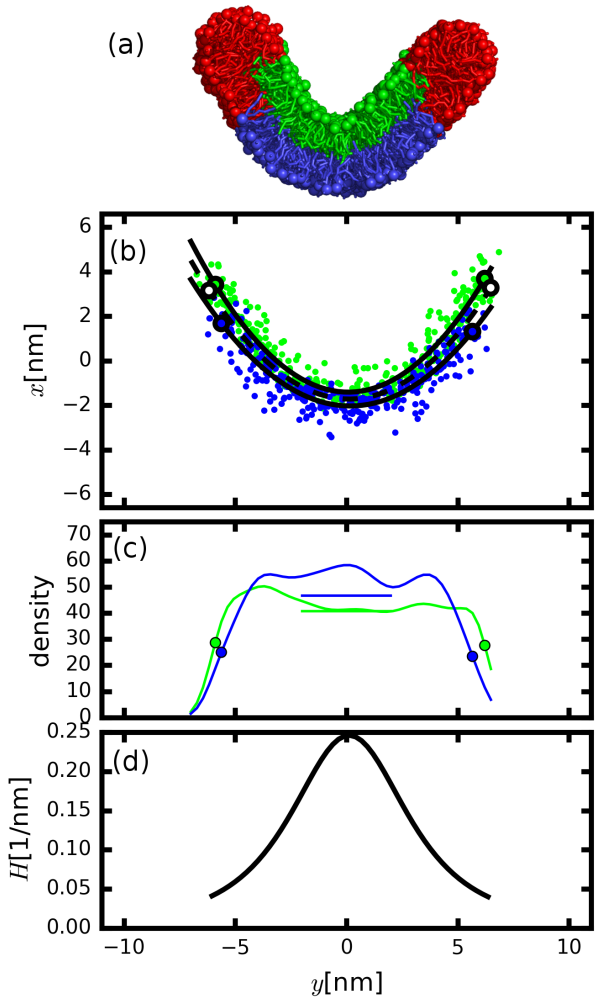

FIG. S10. Computing the midplane surface and its curvature. (a) A representative configuration snapshot for DOPC, taken from the most bent umbrella window. In (a), the 650 restrained lipids are colored green (upper leaflet) and blue (lower leaflet), and unrestrained lipids at the ends are red. (b) The terminal C5A tail beads of the upper (green) and lower (blue) leaflets are plotted as dots. The quadratic fits to single leaflets are shown as solid lines and the endpoints are circles of the corresponding color. The midplane is the dashed line and its endpoints (white circles) are the projections of the upper leaflet's endpoints onto the midplane surface. (c) The C5A bead densities along the top and bottom fit functions. In (c), the horizontal lines indicate the root mean square (RMS) density. The filled circles are the points closest to half the RMS density that are taken as the single leaflet endpoints in (b). (d) The curvature of the midplane surface (dashed line in panel (b)). Due to the parabolic, rather than perfectly cylindrical shape of the bent midplane, the curvature is non-uniform and peaks around 0.25 nm^{-1} (R =4nm) near y =0.

[1] M. Hu, P. Diggins, and M. Deserno, J. Chem. Phys. **138**, 214110 (2013).
[2] S. Baoukina, S. J. Marrink, and D. P. Tieleman, Biophys J **102**, 1866 (2012).
[3] J. Wong-Ekkabut, S. Baoukina, W. Triampo, I.-M. Tang, D. P. Tieleman, and L. Monticelli, Nat Nano **3**, 363 (2008).
[4] Y. G. Smirnova and M. Muller, J. Chem. Phys. **143**, 243155 (2015).
[5] S. J. Marrink, A. H. de Vries, and A. E. Mark, J. Phys. Chem. B **108**, 750 (2004).
[6] S. Shkulipa, *Computer Simulations of Lipid Bilayer Dynamics*, Ph.D. thesis, University of Twente, The Netherlands (2006).
[7] W. K. den Otter and S. A. Shkulipa, Biophys J **93**, 423 (2007).
[8] M. C. Watson, E. S. Penev, P. M. Welch, and F. L. H. Brown, J. Chem. Phys. **135**, 244701 (2011).
[9] M. C. Watson, E. G. Brandt, P. M. Welch, and F. L. H. Brown, Phys. Rev. Lett. **109**, 028102 (2012).
[10] E. G. Brandt, A. R. Braun, J. N. Sachs, J. F. Nagle, and O. Edholm, Biophys J **100**, 2104 (2011).
[11] M. Hu, D. H. d. Jong, S. J. Marrink, and M. Deserno, Faraday Discuss. **161**, 365 (2013).

[12] S. J. Marrink, H. J. Risselada, S. Yefimov, D. P. Tieleman, and A. H. de Vries, J. Phys. Chem. B **111**, 7812 (2007).
[13] B. Hess, C. Kutzner, D. van der Spoel, and E. Lindahl, J. Chem. Theory Comput. **4**, 435 (2008).
[14] J. S. Hub, B. L. de Groot, and D. van der Spoel, J. Chem. Theory Comput. **6**, 3713 (2010).
[15] W. K. den Otter, J. Chem. Phys. **131**, 205101 (2009).
[16] V. A. Harmandaris and M. Deserno, J. Chem. Phys. **125**, 204905 (2006).
[17] I. A. B. Vidal, C. M. Rosetti, C. Pastorino, and M. Muller, J. Chem. Phys. **141**, 194902 (2014).
[18] R. Goetz, G. Gompper, and R. Lipowsky, Phys. Rev. Lett. **82**, 221 (1999).
[19] J. D. Chodera, W. C. Swope, J. W. Pitera, C. Seok, and K. A. Dill, J. Chem. Theory Comput. **3**, 26 (2007).